Supplementary information

Porous Carbon Nanosheets Supported Co Single-Atom Catalysts via Dual-Molten-Salt Synergy for Advanced Zinc-Air Batteries

Qing Long‡ [1,2], Xiaoyan Zhou‡ [1], Jiaxuan Deng‡ [1], Minghong Liu [1], Wu Xia * [3], Junlin Huang* [1], Liang Chen [1], Wenyuan Xu* [1], Hong Yin [1,4], Wei Wang* [1]

[1] *Key Laboratory of Hunan Province for Advanced Carbon-based Functional Materials, School of Chemistry and Chemical Engineering, Hunan Institute of Science and Technology, Yueyang 414006, P. R. China.*

[2] *Institute for Sustainable Transformation, School of Chemical Engineering and Light Industry, Guangdong University of Technology Guangzhou, 510006, P. R. China.*

[3] *College of Chemistry and Chemical Engineering, Jishou University, Jishou 416000, PR China*

[4] *International Iberian Nanotechnology Laboratory (INL), Av. Mestre Jose Veiga, Braga, 4715-330, Portugal.*

‡ These authors contributed equally to this work.

[*]**Corresponding authors**

E-mail addresses: chemxw_2008@163.com (Wu Xia), junlinhuang1022@163.com (Junlin Huang), wenyuanxu@126.com (Wenyuan Xu), ww1454174@foxmail.com (Wei Wang).

Structural Characterization

The sample's Powder X-ray diffraction (XRD) patterns were collected with Cu Kα radiation on a Philips X'pert X-ray diffractometer. The morphology and structural characteristics were examined using scanning electron microscopy (SEM, ZEISS Sigma 300), transmission electron microscopy (TEM, FEITF 20), and high-resolution transmission electron microscopy (HRTEM, FEITF 20) and a high angle annular dark-field scanning TEM (HAADF-STEM, JEOL JEMARM200f). X-ray photoelectron spectroscopy (XPS, Thermo Scientific K-Alpha) was utilized for additional surface composition analysis. Thermal gravimetric analysis (TGA) was performed in air using a PerkinElmer STA-8000 thermal analyzer within the temperature range of 30 °C to 800 °C at a heating rate of 10 °C min^{-1}. Raman spectra were obtained using a Raman spectrometer (DXRxi). The specific surface area was determined through N_2 adsorption/desorption analysis at 77 K using a Micromeritics ASAP 2020 HD analyzer. X-ray absorption fine structure (XAFS) measurements were performed at the BL14W beamline of the Shanghai Synchrotron Radiation Facility (SSRF) (Shanghai, China) in fluorescence excitation mode. The device operates with an Ag X-ray tube source and is equipped with a silicon drift detector (AXAS-M1, KETEK GmbH).

Electrocatalytic measurements

The ORR electrochemical measurements were conducted using a CHI760E workstation with a three-electrode setup and a 0.1 M KOH solution as the electrolyte. The working electrode was a platinum rod, and the reference electrode was Ag/AgCl. Calibration was performed based on the reversible hydrogen electrode (RHE) equation at 25 °C. A glassy carbon electrode (GCE) with a 5 mm diameter, coated with a thin catalyst film, was used as the working electrode. The catalyst ink was prepared by mixing 5 mg of catalyst with 980 μL of ethanol and 20 μL of Nafion solution. 15.7 μL of the catalyst ink was applied to the GCE and dried using a light bulb, resulting in a catalyst loading of 400 μg cm^{-2}. For comparison, Pt/C (20%, ETEK) with a loading of 300 μg cm^{-2} was also tested. Linear sweep voltammetry (LSV) was carried out at a rate of 50 mV s^{-1} in an O_2-saturated electrolyte at 1600 rpm. Chronoamperometry (i-t) was performed at 0.6

V and 1600 rpm in an O_2-saturated electrolyte to evaluate the stability and methanol tolerance of the samples. All current values were converted to current density during the experiments.

Koutecky-Levich equation

In the calculation of the number of transferred electrons (n) for each oxygen molecule during the ORR process, the Koutecky-Levich equation utilizes the slope of the best linear fitting line.

$$\frac{1}{J} = \frac{1}{J_L} + \frac{1}{J_K} = \frac{1}{Bw^{1/2}} + \frac{1}{J_K} \quad (1)$$

$$B = 0.2nFC_0(D_0)^{2/3}v^{-1/6} \quad (2)$$

Where J (mA cm^{-2}) is the measured current density, J_K (mA cm^{-2}) and J_L (mA cm^{-2}) denote the kinetic and diffusion-limiting current densities respectively, ω is the electrode rotation rate (rpm), n is the electron transfer number in oxygen reduction, F is the Faraday constant (F=96485C mol^{-1}), C_0 is the bulk concentration of O_2 (C_0=1.2×10^{-6} mol cm^{-3}), D_0 is the diffusion coefficient of O_2 (1.93 × 10^{-5} cm^2 s^{-1}), ν is the kinematic viscosity of the electrolyte (0.01 cm^2 s^{-1}), The constant 0.2 is adopted when the rotating speed is in rpm.

Randles-Sevcik equation

To compare the apparent diffusion coefficients (D) of O_2 during the ORR process for each sample, linear fitting was performed using the Randles-Sevcik equation:

$$i_p = (2.69\times10^5)n^{3/2}SD^{1/2}Cv^{1/2} \quad (3)$$

where n is the number of electrons transferred, i_p is the peak current, S is the electrode area, D is the apparent diffusion coefficient of O_2, C is the saturated concentration of O_2, and v is the scan rate.

Zn-Air battery measurements

The solid zinc-air battery was constructed using a carbon cloth (2 cm × 2.5 cm) loaded with a catalyst (1 mg cm^{-2}) as the cathode, and a polished zinc sheet as the anode. The

electrolyte contained 11.25 M KOH gel with the addition of 0.25 M ZnO. The battery underwent testing using the LAND and CHI electrochemical workstations.

For the liquid zinc-air battery tests, a homemade battery was used with a zinc plate (3 cm × 8 cm) as the anode. The air-electrode was created by drop-casting a catalyst ink (9 mg mL^{-1}) onto carbon paper (3 cm × 3 cm) with a copper-foam current collector. The zinc-air battery was then assembled by filling the electrolyte (6 M KOH and 0.2 M $Zn(Ac)_2$) between the anode and air-cathode.

Computational details

The density of states (DOS) and electron density difference of Co-NCPC-800 and Co-DNC-2 were calculated by using quantum chemical calculation method based on the density functional theory (DFT) of CASTEP module (Materials Studio 8.0, BIOVIA, San Diego, US). The generalized gradient approximation (GGA) method with Perdew-Burke-Ernzerhof (PBE) functional for the exchange-correlation term was used. A plane-wave basis set with an energy cutoff of 300 eV and 2×2×1 k-point sampling was used for Brillouin zone (BZ). The electronic and ionic convergence criteria were respectively set to 10^{-5} eV and 0.03 eV·$Å^{-1}$, and all calculations were performed spin-polarized. In the calculations, geometry optimization of all the atoms in the structure were performed.

The adsorption energy value of O_2 (ΔE_{ad}) were calculated according to

$$\Delta E_{ad} = E_{ad}* - E_{surface} - E_{ad} \quad (4)$$

where $E_{ads}*$ is the surface with adsorbed O_2 molecule, while $E_{surface}$ and E_{ads} represent the energies of the materials surface model and isolated O_2 molecule, respectively.

In general, the four-electron ORR pathway can be described as:

$$* + O_2 + H_2O + e^- \rightarrow OOH* + OH^- \quad (5)$$

$$OOH* + e^- \rightarrow O* + OH^- \quad (6)$$

$$O* + H_2O + e^- \rightarrow OH* + OH^- \quad (7)$$

$$OH* + e^- \rightarrow OH^- + * \quad (8)$$

where * stands for the adsorption site on catalysts surface. OOH*, O* and OH* are the

ORR intermediates.

The Gibbs reaction free energy (ΔG) is the difference between the free energy of the initial and final states and can be calculated from the following equation:

$$\Delta G_{ads} = \Delta E_{ads} + \Delta ZPE_{ads} - T\Delta S_{ads} + \Delta G_U + \Delta G_{pH} \quad (9)$$

where ΔE_{ads} is the reaction energy change and adsorption energy of oxygen species. ΔE_{ads} can be calculated according to equation (4) mentioned earlier. ΔZPE and ΔS refer to the zero-point energy and entropic energy of the adsorption molecule, respectively. ΔG_U = -neU, where U is the electrode applied potential relative to RHE as mentioned above, e is the elementary charge transferred and n is the number of proton-electron pairs transferred. ΔGpH = pH × k_B T ln10, where k_B is the Boltzmann constant and T is the application temperature (298.15 K).

The reaction free energy of equations (5)-(8) (ΔG_1, ΔG_2, ΔG_3, ΔG_4) for ORR can be calculated using the following equations:

$$\Delta G_1 = \Delta G_{*OOH} - 4.92 \quad (10)$$

$$\Delta G_2 = \Delta G_{*O} - \Delta G_{*OOH} \quad (11)$$

$$\Delta G_3 = \Delta G_{*OH} - \Delta G_{*O} \quad (12)$$

$$\Delta G_4 = -\Delta G_{*OH} \quad (13)$$

The *d* band center (ε_d) of Fe atom is calculated by following equation:

$$\varepsilon_d = \int_{-\infty}^{\infty} x\rho(x)dx \Big/ \int_{-\infty}^{\infty} \rho(x)dx \quad (14)$$

where the $\rho(x)$ refers to the d-typed PDOS of the corresponding Co atom.

Figure and captions

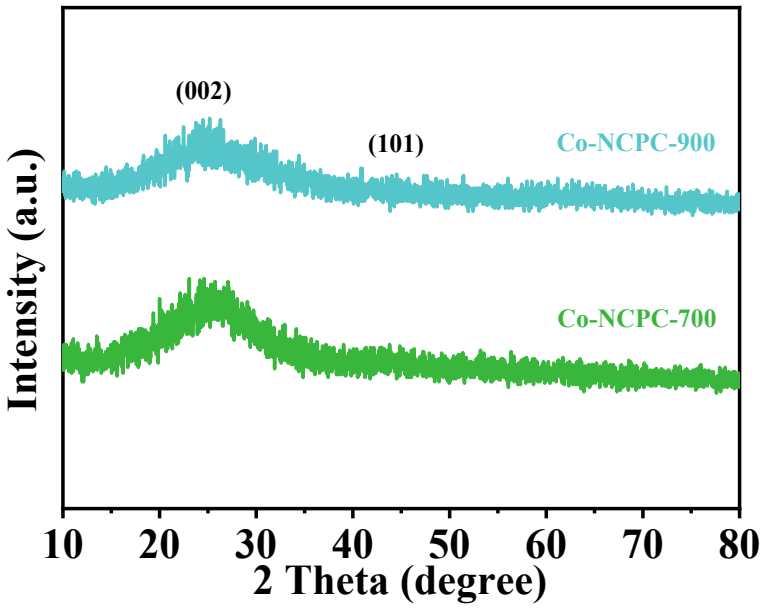

Fig. S1 XRD patterns of Co-NCPC-700, Co-NCPC-900.

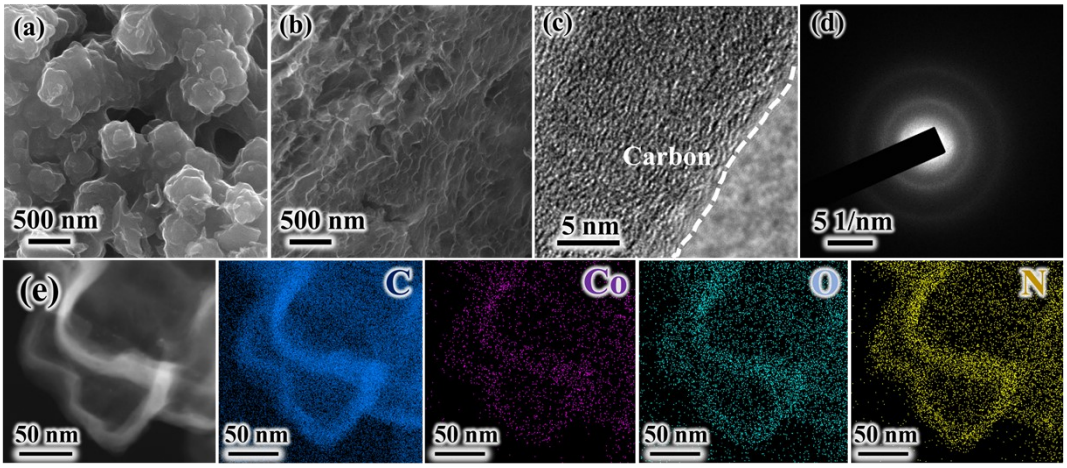

Fig. S2 (a-b) SEM of Co-NCPC-700, Co-NCPC-900. (c-d) HRTEM image and SAED patterns of Co-NCPC-800. (e) High angle annular dark field image and the elemental mapping of Co-NCPC-800.

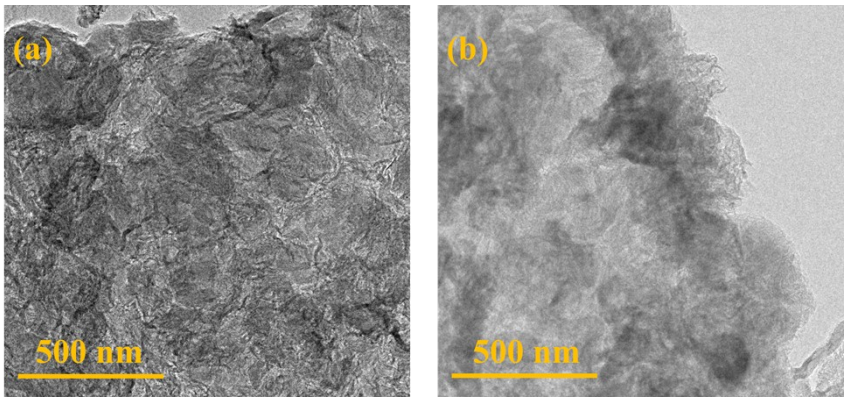

Fig. S3 (a-b) TEM of Co-DNC-2.

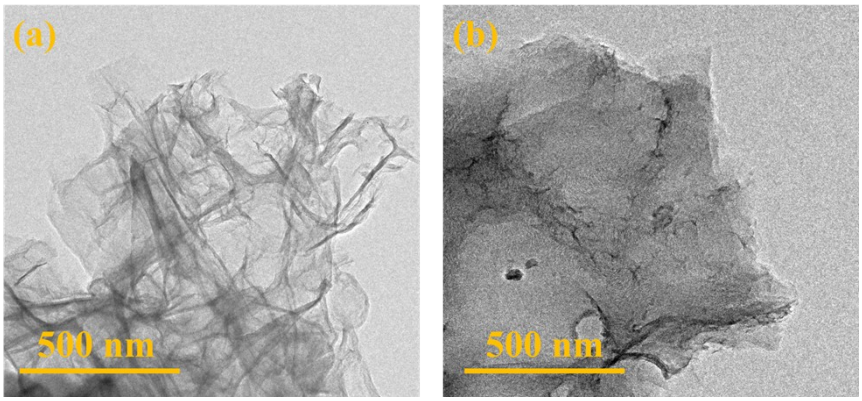

Fig. S4 (a-b) TEM of Co-NCPC-800.

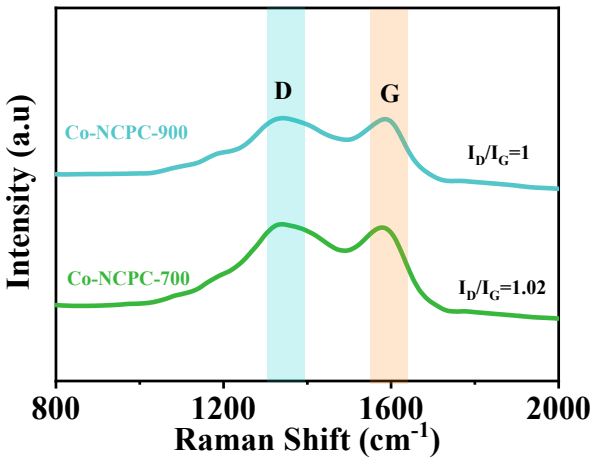

Fig. S5 Raman spectra of Co-NCPC-700, Co-NCPC-900.

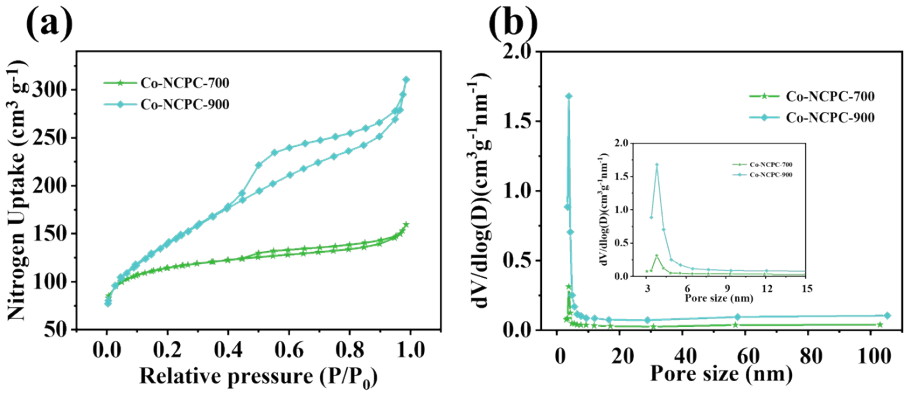

Fig. S6 (a-b) N_2 adsorption/desorption isotherms and pore size distribution curves of the Co-NCPC-700, Co-NCPC-900.

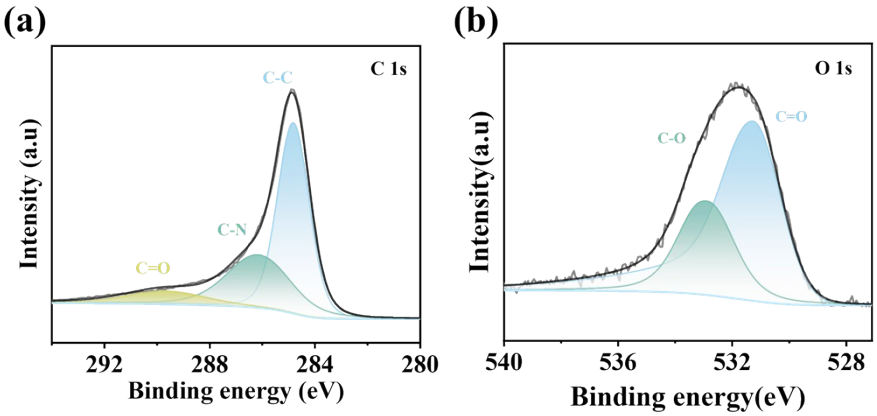

Fig. S7 High-resolution spectra of (a) C 1s, (b) O 1s for Co-DNC-2.

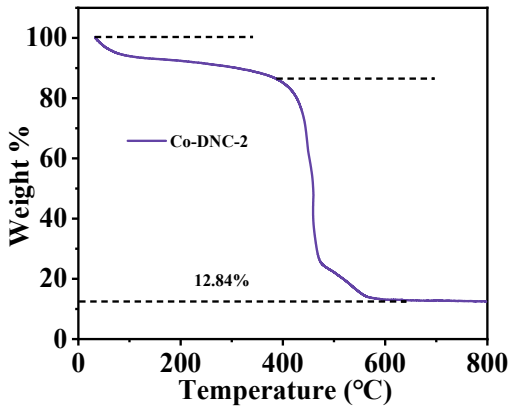

Fig. S8 TG curve of Co-DNC-2 under air atmosphere.

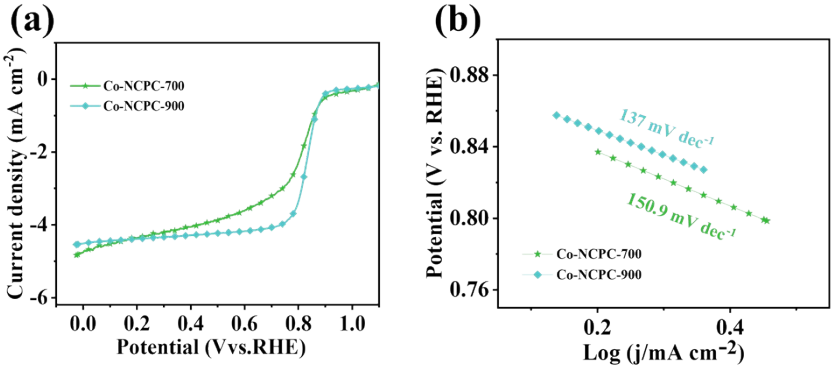

Fig. S9 (a) LSVs at 1600 rpm in O_2-saturated 0.1 M KOH of Co-NCPC-700, Co-NCPC-900. (b) The corresponding Tafel slope at 1600 rpm of Co-NCPC-700, Co-NCPC-900.

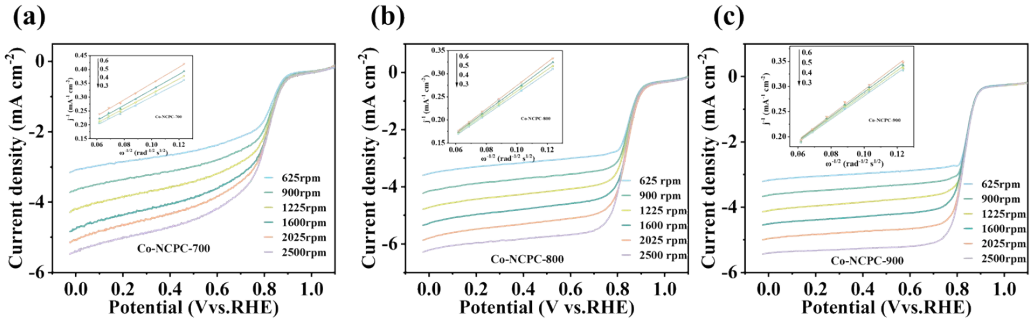

Fig. S10 The LSVs of of (a) Co-NCPC-700, (b) Co-NCPC-800, (c) Co-NCPC-900 at different rotation rates. The inset shows the corresponding K-L plots.

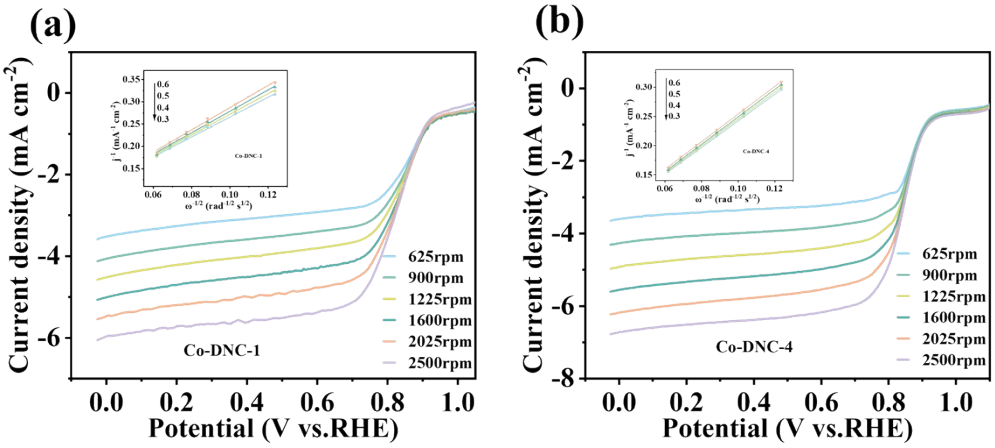

Fig. S11 The LSVs of of (a) Co-DNC-1, (b) Co-DNC-4 at different rotation rates. The inset shows the corresponding K-L plots.

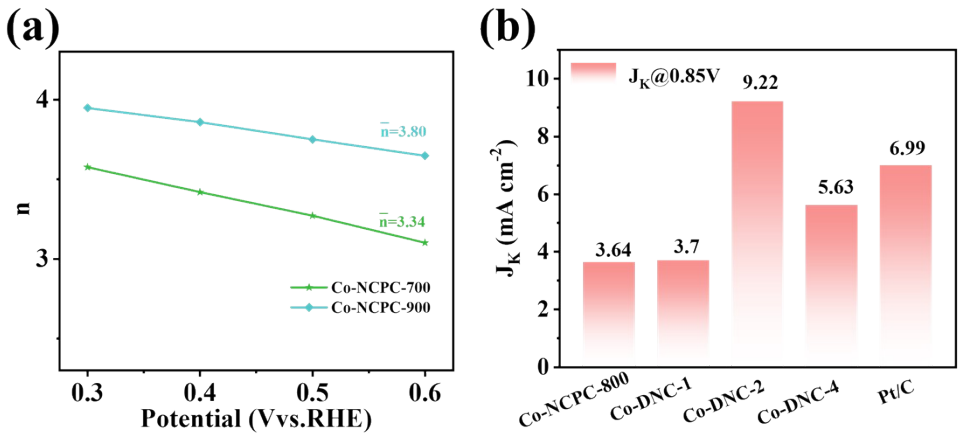

Fig. S12 (a) Transferred electron number of Co-NCPC-700, Co-NCPC-900. (b) J_k of Co-NCPC-800, Co-DNC-X and Pt/C at 0.85 Vvs.RHE.

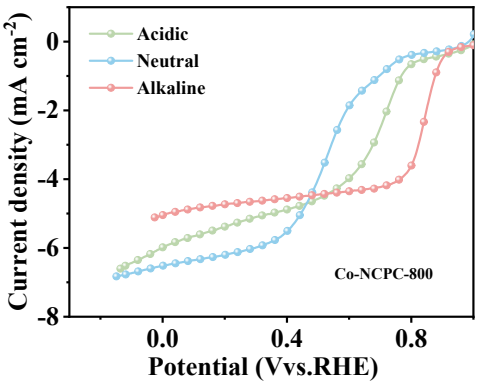

Fig. S13 (a) LSVs at 1600 rpm in O_2-saturated 0.1 M KOH, 1M PBS, 0.1 M $HClO_4$.

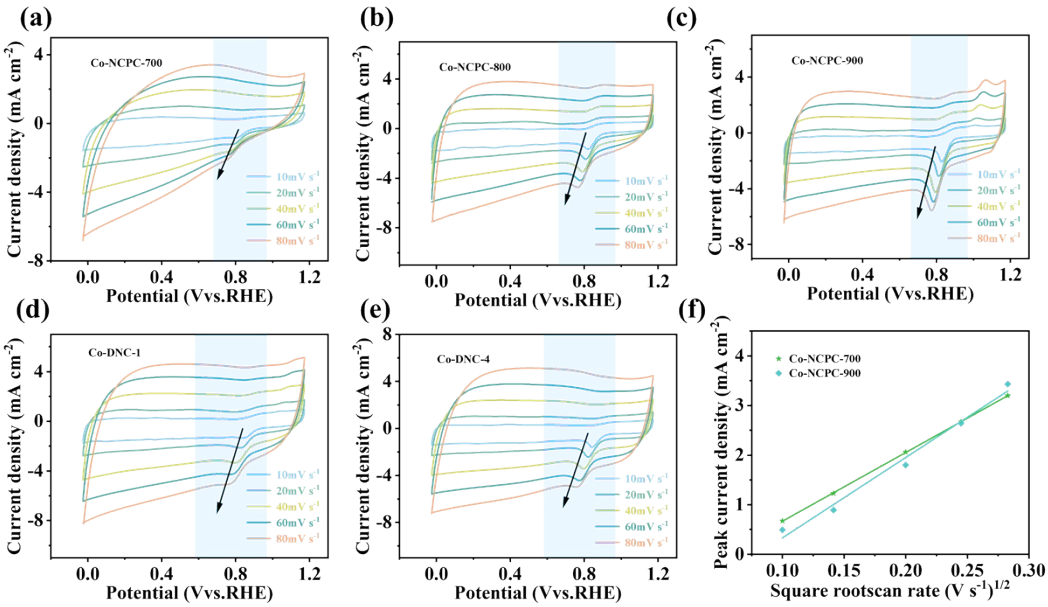

Fig. S14 (a-e) CV curves on Co-NCPC-X, Co-DNC-1, Co-DNC-4 electrodes at various scan rates. (f) The peak current density (i_p) versus square root of scan rate plot.

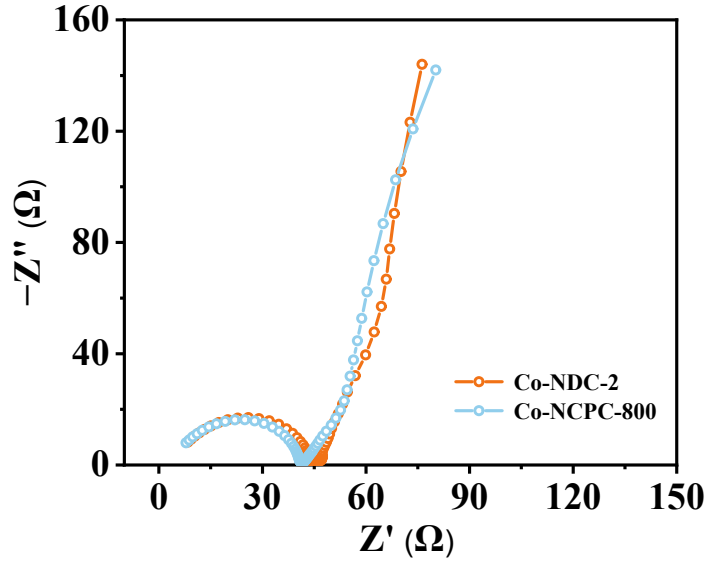

Fig. S15 Nyquist plots of Co-NCPC-800, Co-DNC-2

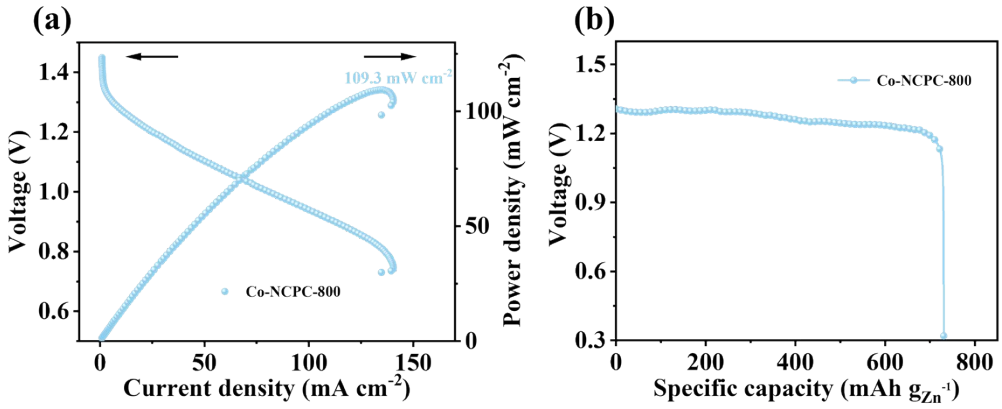

Fig. S16 (a) Discharge polarization and power density curves of solid-state ZABs. (b) Discharge curves of solid-state ZABs at 5 mA cm^{-2}.

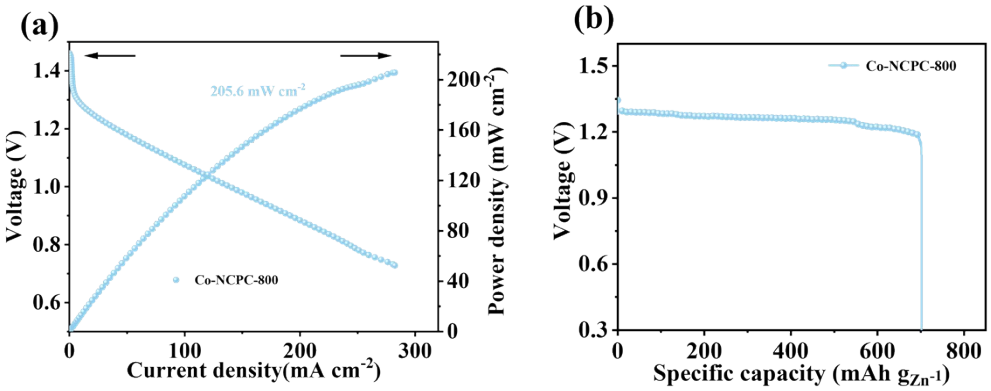

Fig. S17 (a) Discharge polarization and power density curves of liquid ZABs. (b) Discharge curves of liquid ZABs at 5 mA cm^{-2}.

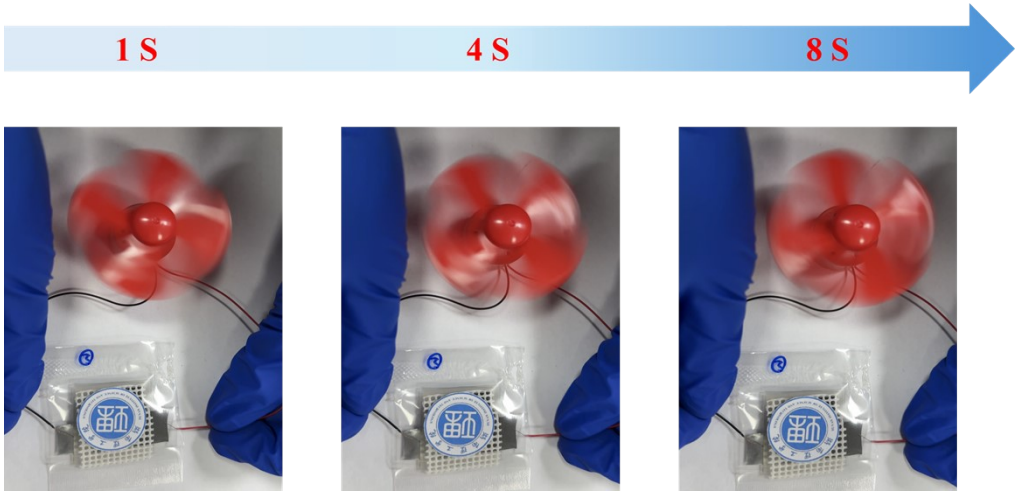

Fig. S18 Schematic diagram of a solid-state zinc-air battery based on Co-DNC-2 for powering a small fan.

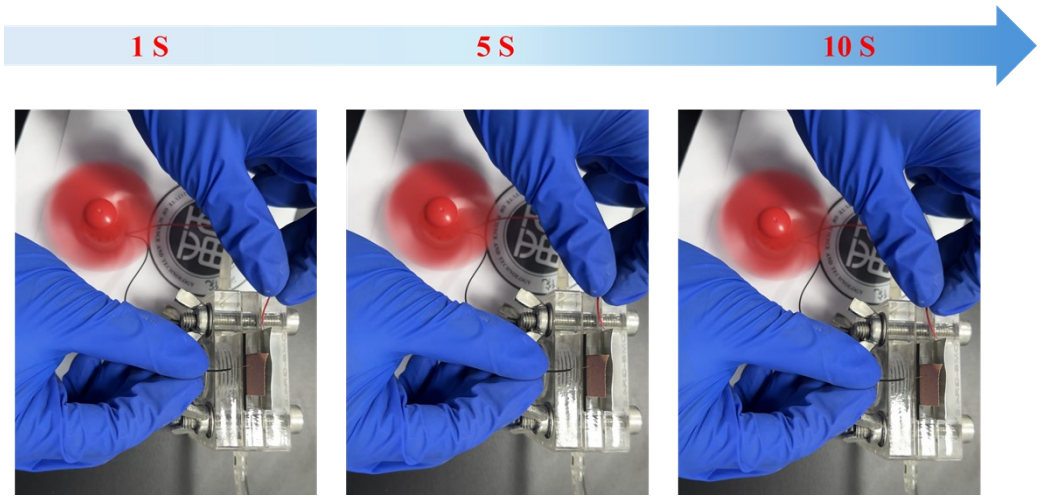

Fig. S19 Schematic diagram of a liquid zinc-air battery based on Co-DNC-2 for powering a small fan.

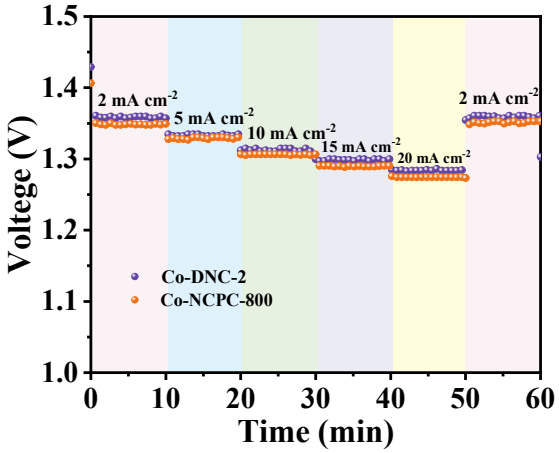

Fig. S20 Discharge curves of Co-DNC-2 and Co-NCPC-800 under serial current densities.

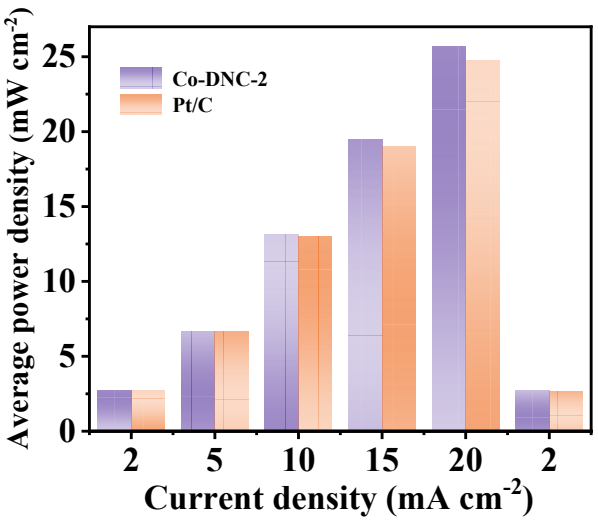

Fig. S21 Comparison of average power of liquid ZABs at different current densities discharge curves.

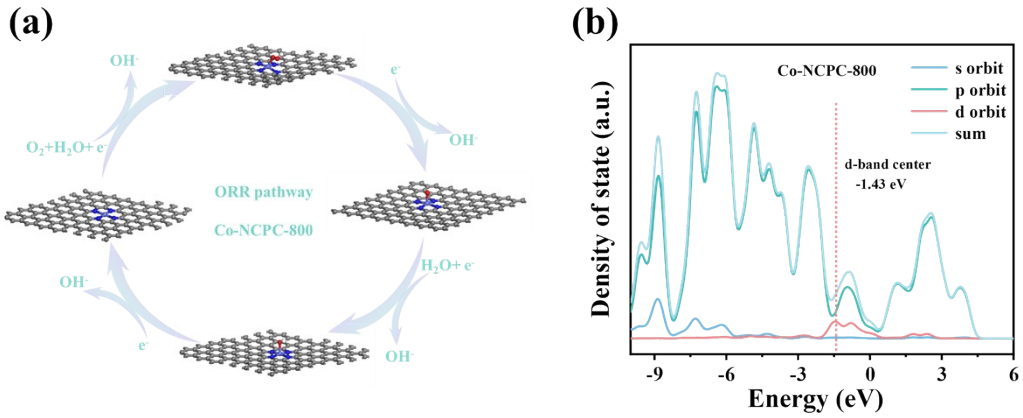

Fig. S22 (a) schematic ORR process on the Co-N_x site. (b) DOS of Co-NCPC-800 model.

Tabel. S1 Comparison of Performance Characteristics for Zinc-Air Batteries Based on Co-DNC-2, Co-NCPC-800 and Pt/C.

Sample	Power density (mW cm^{-2}) (solid-state ZABs)	Power density (mW cm^{-2}) (liquid-state ZABs)	Specific capacity (mA h g_{Zn}^{-1}) (solid-state ZABs)	Specific capacity (mA h g_{Zn}^{-1}) (liquid-state ZABs)
Co-NCPC-800	109.3	205.6	730.8	701.7
Co-DNC-2	123.6	240.5	773.6	752.4
Pt/C	97.6	161.1	703.7	680.8